Döhmann, M., Brune, S., Nardini, L., Rybacki, E., Dresen, G. (2019): Strain Localization and Weakening Processes in Viscously Deforming Rocks: Numerical Modeling Based on Laboratory Torsion Experiments. - *Journal of Geophysical Research*, *124*, 1, pp. 1120—1137.

DOI: http://doi.org/10.1029/2018JB016917

JGR Solid Earth

RESEARCH ARTICLE
10.1029/2018JB016917

# Strain Localization and Weakening Processes in Viscously Deforming Rocks: Numerical Modeling Based on Laboratory Torsion Experiments

M. J. E. A. Döhmann[1,2], S. Brune[1,2], L. Nardini[1], E. Rybacki[1], and G. Dresen[1,2]

[1]Helmholtz-Centre Potsdam-GFZ German Research Centre for Geosciences, Potsdam, Germany, [2]Institute of Earth and Environmental Sciences, University of Potsdam, Potsdam, Germany

**Key Points:**
- First-order numerical softening laws successfully reproduce strain localization and stress transients observed in laboratory torsion tests
- Our models provide a virtual way of analyzing viscous process zone evolution as it nucleates near an inclusion and propagates into a matrix
- The degree of weakening controls the process zone geometry, the finite width of shear bands, and the potential formation of ultramylonites

**Supporting Information:**
- Supporting Information S1

**Correspondence to:**
M. J. E. A. Döhmann,
doehmann@gfz-potsdam.de

**Citation:**
Döhmann, M. J. E. A., Brune, S., Nardini, L., Rybacki, E., & Dresen, G. (2019). Strain localization and weakening processes in viscously deforming rocks: Numerical modeling based on laboratory torsion experiments. *Journal of Geophysical Research: Solid Earth*, *124*, 1120–1137. https://doi.org/10.1029/2018JB016917

Received 20 OCT 2018
Accepted 8 JAN 2019
Accepted article online 12 JAN 2019
Published online 30 JAN 2019



**Abstract** Localization processes in the viscous lower crust generate ductile shear zones over a broad range of scales affecting long-term lithosphere deformation and the mechanical response of faults during the seismic cycle. Here we use centimeter-scale numerical models in order to gain detailed insight into the processes involved in strain localization and rheological weakening in viscously deforming rocks. Our 2-D Cartesian models are benchmarked to high-temperature and high-pressure torsion experiments on Carrara marble samples containing a single weak Solnhofen limestone inclusion. The models successfully reproduce bulk stress-strain transients and final strain distributions observed in the experiments by applying a simple, first-order softening law that mimics rheological weakening. We find that local stress concentrations forming at the inclusion tips initiate strain localization inside the host matrix. At the tip of the propagating shear zone, weakening occurs within a process zone, which expands with time from the inclusion tips toward the matrix. Rheological weakening is a precondition for shear zone localization, and the width of this shear zone is found to be controlled by the degree of softening. Introducing a second softening step at elevated strain, a high strain layer develops inside the localized shear zone, analogous to the formation of ultramylonite bands in mylonites. These results elucidate the transient evolution of stress and strain rate during inception and maturation of ductile shear zones.

## 1. Introduction

Localization of deformation is ubiquitous in Earth materials and observed over a broad range of scales in space and time (Fossen & Cavalcante, 2017). In the brittle upper crust, localization is represented by fault zones (Coyan et al., 2013; Valoroso et al., 2013) transitioning into localized ductile shear zones in the middle-lower crust at the brittle-ductile transition hosting mylonites and ultramylonites (Palin et al., 2014; Park & Jung, 2017). Localization within the deeper ductile lithosphere is accommodated by a combination of different deformation mechanisms, for example, diffusion and dislocation creep, frictional sliding, or cataclasis, depending on mineral composition and boundary conditions (Burlini & Bruhn, 2005; Kenkmann & Dresen, 2002). These processes cause shear zone initiation at material heterogeneities and multiple defects commonly present in rocks that serve as nucleation points for shear zones on the microscle or macroscale. Typical examples include randomly scattered flaws (e.g., Misra & Mandal, 2007), brittle fractures (Mancktelow & Pennacchioni, 2005), weak layers (Gerbi et al., 2015), veins and dykes (Handy, 1989), or rock fabric (Bürgmann & Dresen, 2008). A plethora of studies showed that a subsequent strength reduction in shear zones may be attributed to a wide range of processes, like grain size reduction (Tasaka et al., 2017), shear heating (Duretz et al., 2015), a combination of both (Foley, 2018), a change in controlling deformation mechanism such as from dislocation to diffusion creep (e.g., Handy, 1989; Linckens et al., 2011; White, 1976), and the development of crystallographic preferred orientations (Ji et al., 2004) or melting (Handy et al., 2001).

Laboratory experiments on rock materials provide insights into localization and weakening processes during shear zone formation at well-defined deformation conditions. Several experimental studies at high P-T conditions have investigated strength and microstructures in high-strain deformation tests on monomineralic geomaterials. For pure Carrara marble it was found that strain weakening is associated with recrystallization to a fine grain size, the development of a strong lattice-preferred orientation (Pieri, Burlini, et al., 2001), and that steady state flow is reached at shear strains $\gamma > 4$ (Pieri, Kunze, et al., 2001).

In axial compression tests at 700–990 °C, Ter Heege et al. (2001) found that dislocation creep mechanisms dominate Carrara marble flow at peak stresses and that grain size sensitive mechanisms contribute to flow only for higher bulk shear strains. However, Barnhoorn et al. (2004) observed no significant contribution of diffusion creep even for large shear strains $\gamma \leq 50$. Only minor rheological weakening may be attributed to grain size reduction by dynamic recrystallization, if grain growth is not inhibited (De Bresser et al., 2001). Zener pinning, for example, impedes grain growth and can thus enhance strain localization (Bercovici & Ricard, 2012; Bruhn et al., 1999; Herwegh et al., 2005; Linckens et al., 2011). By means of experimental studies with multiphase aggregates the localization phenomena have been analyzed at various conditions. A second phase, for example, helps maintain a fine grain size that allows continuous deformation in the diffusion creep regime (Tasaka et al., 2017). Geometric phase mixing occurs only at very high shear strains and is hence a consequence of localization (Cross & Skemer, 2017). Stress partitioning in a two phase system may lead to above-average stresses in one phase and comparatively low stresses in the other (Bruhn & Casey, 1997). Strong stress and strain gradients close to matrix/inclusion interfaces were also observed in a two-phase study using anorthite-diopside aggregates and are similar to deformation microstructures observed in ultramylonites (Dimanov & Dresen, 2005). The effect of material heterogeneities on the rheological response of otherwise homogeneous Earth materials has been recently addressed by Rybacki et al. (2014), who analyzed the effect of material heterogeneities on the onset of localized viscous deformation. These studies revealed a rich interplay of various factors and processes, yet it is difficult to study individual processes in isolation and to provide a time-dependent view of strain localization.

In addition to experimental studies, numerical modeling of localization processes allows testing realistic materials in order to isolate the effect of specific deformation mechanisms and parameters. Previous numerical modeling work aimed at understanding the role of strength anisotropies that are either caused by compositional differences (Cook et al., 2014; Kenkmann & Dresen, 1998; Mancktelow, 2002; Treagus & Lan, 2004) or due to inherited structures (Corti et al., 2007; Mazzotti & Gueydan, 2018; Webber et al., 2018). For example, during lithospheric extension the inherited mechanical structure exerts a strong control on rift geometry and architecture (Duretz et al., 2016). Material heterogeneities significantly impact strain localization: (1) hard inclusions produce stress concentrations inside a homogeneous matrix (Kenkmann & Dresen, 1998) and (2) weak inclusions localize strain in turn producing stress concentrations at the inclusion matrix interface (Cyprych et al., 2016). Jammes et al. (2015) identified three end-member types of shear zones: (1) localized, (2) localized anastomosing, and (3) delocalized shear zone that depend on the proportion of strong and weak phase and the strength ratio. Other modeling studies focused on the effect of rheological weakening and hardening mechanisms. Weakening mechanisms have been formulated as a function of strain (Cyprych et al., 2016; Mazzotti & Gueydan, 2018), stress (Gardner et al., 2017), and deformation work or grain size in combination with grain size-dependent flow laws (e.g., Bercovici & Ricard, 2012; Cross et al., 2015; Herwegh et al., 2014; Jessell et al., 2005). However, all these formulations have been shown to strongly influence the localization behavior in numerical models.

Here we compare the results of our numerical models to a series of laboratory tests (Nardini et al., 2018), in order to investigate the temporal and spatial evolution of strain localization and weakening processes in viscously deforming rocks. As mentioned above, ductile shear zones are often initiated at material heterogeneities, which is why we use a single weak inclusion torsion setup to analyze dynamics, strength, and geometry of the resulting ductile shear zone. Based on this reference model, we perform additional numerical experiments assessing the time-dependent impact of weakening through a scan of the relevant parameters and finally we focus on the formation of ultramylonites.

## 2. Laboratory Experiments

### 2.1. Experimental Setup

Sample preparation is following the procedures described in Rybacki et al. (2014): Cylinders of Carrara marble (10 mm in length, 15-mm outer diameter) were cut from a single block of marble, and an internal borehole (6.1 mm of inner diameter) was cored and subsequently filled with cylinders of solid gold to provide a homogeneous distribution of stress over the entire sample through the full duration of the experiments (Paterson & Olgaard, 2000). Circular segments of Solnhofen limestone (arc length ~11.8 mm), a very fine

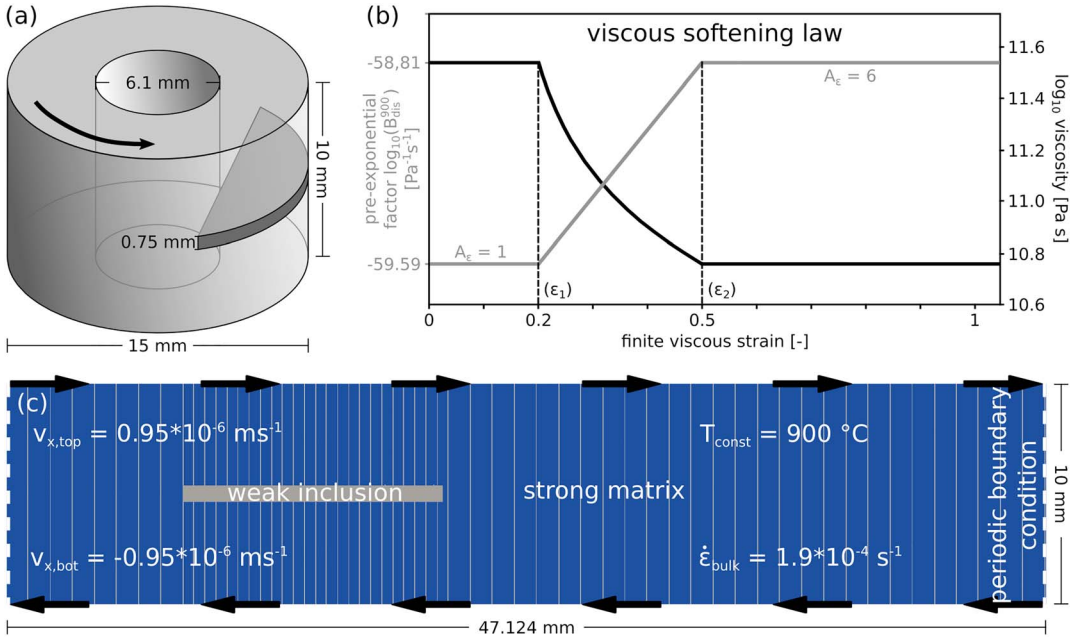


**Figure 1.** (a) Schematic drawing of experimental setup: cylinder height is 10 mm, outer diameter is 15 mm, the inclusion features an angular length of 90°, and the inner borehole has a diameter of 6.1 mm and is filled with a solid gold cylinder. The matrix consists of Carrara marble and the inclusion of Solnhofen limestone. (b) Effect of viscous softening on Carrara marble flow law. The factor $A_\varepsilon$ (a fraction of the weakening amplitude $A$) is increased between the two threshold values of local finite strain $\varepsilon_1$ and $\varepsilon_2$; hence, the effective viscosity is locally reduced. (c) Model setup and boundary conditions. Constant bulk strain rate ($\dot{\varepsilon}_{bulk}$) is achieved by prescribing velocity at top ($v_{x,\ top}$) and bottom ($v_{x,\ bot}$) model boundaries. At the left and right model side we use periodic boundary conditions, that is, velocity and stress are continuous across these faces and any material point crossing these boundaries enters again on the other side of the model. Flow laws of matrix and inclusion are chosen to represent Carrara marble (strong matrix) and Solnhofen limestone (weak inclusion; see Table 1). Vertical gray lines are passive strain markers.

grained (average grain size <10 μm) rock, were produced by polishing ~750-μm thick sections that were subsequently inserted in the external surface of the Carrara marble cylinders (see Figure 1a).

Experiments were conducted in a Paterson-type gas deformation apparatus (Paterson, 1970), at 900 °C temperature and 400-MPa confining pressure. The samples were inserted in copper jackets of ~0.2-mm thickness, and jacket strength at the experimental conditions was accounted for in the evaluation of the mechanical data. Straight vertical scratches on the jacket surface serve as passive strain markers. As shown in Rybacki et al. (2014), at experimental P-T conditions the fine grained limestone is substantially softer than Carrara marble and therefore acts as a weak material heterogeneity within a homogeneous stronger matrix. Two different loading conditions, constant twist rate (equivalent to a shear strain rate of $1.9 \times 10^{-4}\ s^{-1}$ at the outer periphery) and constant torque (~18.8 MPa) were tested. For each loading type, samples were tested to a final bulk shear strain $\gamma \sim 1$ (Nardini et al., 2018).

### 2.2. Experimental Results

At constant twist rate, calculated shear stress at the sample periphery initially increased up to a peak value of ~19–20 MPa at a bulk shear strain of $\gamma \sim 0.2$, followed by gradual weakening up to the maximum bulk shear strain of about 1 for sample CTR1 (Figure 2a). This sample is used to benchmark the numerical model. In the constant torque experiment, torque was kept uniform such that the maximum shear stress at the sample periphery was about 18.8 MPa, similar to the peak stress measured in the constant twist rate experiment (see supporting information Figure S1 for results of the constant torque experiment and a comparison to a numerical model). The experiments reveal that in front of the inclusion the strain within the Carrara marble was strongly localized forming a *process zone* consisting of highly deformed grains and grain size reduction. The local shear strain in this area is higher than in the adjacent host rock. At the inclusion tip, the local strain

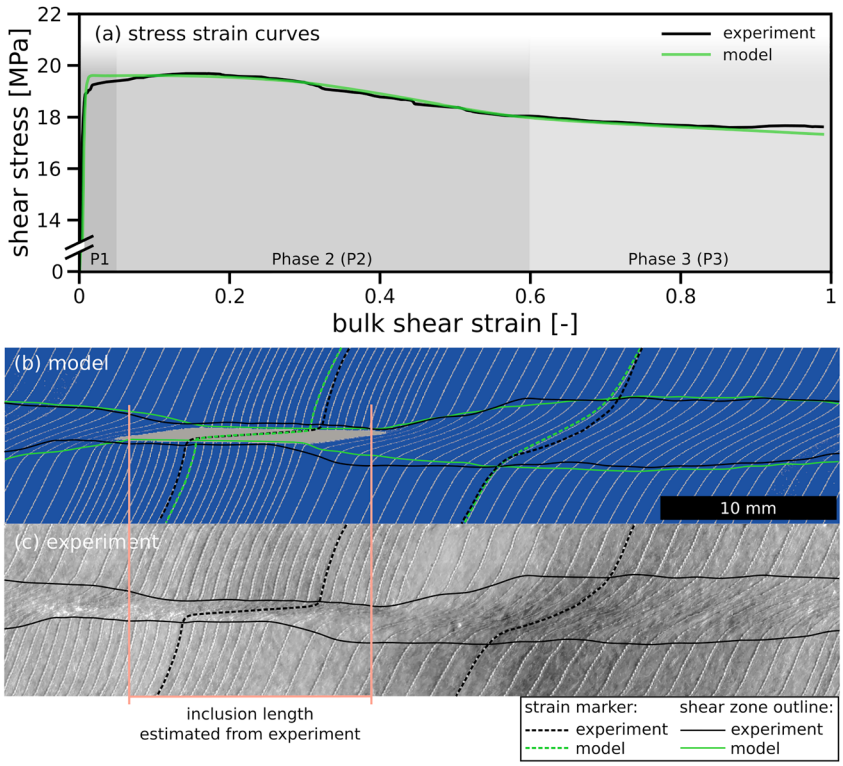


**Figure 2.** Benchmark and comparison of constant strain rate model to experiment. (a) Stress strain curves of reference model (green) and experiment (black). Background shows the phases P1—preweakening, P2—onset and acceleration of weakening, and P3—deceleration of weakening. (b) Model with passive strain markers and shear zone outlines of model (green) and experiment (black). (c) Copper jacket from experiment with passive strain markers, estimated inclusion length and shear zone outline. Results in (b) and (c) are shown at a bulk shear strain of ~1.

is up to about 30 times higher than in the neighboring matrix and ~10 times higher than the bulk strain (Nardini et al., 2018).

## 3. Model Description

In the following, we describe the setup of the numerical model and examine (i) the results in comparison to the associated laboratory experiments, (ii) the time-dependent evolution of the model, (iii) the role of softening, (iv) the effect of varying softening parameters, and (v) the impact of progressive softening. Points (i) and (ii) combined with the mechanical data yield further insights into the strain localization process. With (iii) to (v) we expand the parameter space beyond the experimental results allowing new insights from the numerical perspective.

### 3.1. Numerical Modeling Technique

We use the geodynamic modeling software SLIM3D (Semi-Lagrangian Implicit Model for 3 Dimensions; Popov & Sobolev, 2008). The implicit finite element code utilizes the Arbitrary Lagrangian-Eulerian Method has a realistic elasto-visco-plastic formulation for rheology and a free surface. The software was originally designed to investigate lithospheric-scale processes and has since been applied in divergent (Brune, 2014; Brune et al., 2012, 2013, 2014, 2016, 2017; Brune & Autin, 2013; Clift et al., 2015; Heine & Brune, 2014; Koopmann et al., 2014), convergent (Ballato et al., 2019; Duesterhoeft et al., 2014; Quinteros et al., 2010; Quinteros & Sobolev, 2013), and transform (Brune, 2014; Popov et al., 2012) plate boundary settings. Recently, however, its scope has been extended with the aim to investigate localization processes on the centimeter scale (Cyprych et al., 2016).

With the SLIM3D software, we solve the thermomechanically coupled conservation equations of momentum

$$-\frac{\partial p}{\partial x_i}+\frac{\partial \tau_{ij}}{\partial x}+\rho g_z=0 \tag{1}$$

energy

$$\rho C_p\frac{DT}{Dt}-\frac{\partial}{\partial x_i}\left(\lambda\frac{\partial T}{\partial x_i}\right)-\tau_{ij}\dot{\varepsilon}_{ij}=0 \tag{2}$$

and mass

$$\frac{1}{K}\frac{Dp}{Dt}-\alpha_T\frac{DT}{Dt}+\frac{\partial v_i}{\partial x_i}=0 \tag{3}$$

with coordinates $x_i$, velocities $v_i$, temperature $T$, time $t$, pressure $p$, stress deviator $\tau_{ij}$, strain rate deviator $\dot{\varepsilon}_{ij}$, densities $\rho$, gravity vector $g_z$, heat capacities $C_p$, heat conductivities $\lambda$, thermal expansivities $\alpha_T$, and bulk moduli $K$. The Einstein summation convention is applied over repeated indices.

The conservation equations are solved simultaneously considering the constitutive laws that relate deformation and stress. Total deviatoric strain rate is described as the sum of elastic and viscous strain rate (Simo & Hughes, 2006):

$$\dot{\varepsilon}_{ij}=\dot{\varepsilon}_{ij}^{\text{elastic}}+\dot{\varepsilon}_{ij}^{\text{viscous}}=\frac{1}{2G}\hat{\tau}_{ij}+\frac{1}{2\eta_{\text{eff}}}\tau_{ij} \tag{4}$$

where $G$ is the elastic shear modulus, $\hat{\tau}_{ij}$ the objective stress rate (e.g., Bonet & Wood, 1997), and $\eta_{\text{eff}}$ the effective viscosity.

We use dislocation creep flow laws to model the viscous deformation of limestone and marble. The effective viscosity is described as

$$\eta_{eff}=\frac{1}{2}\tau_{II}\dot{\varepsilon}_{\text{dis}}^{-1} \tag{5}$$

with $\tau_{II}$ as the second invariant of the effective deviatoric stress given by

$$\tau_{II}=\sqrt{\frac{1}{2}(\sigma_{xx}-p)^2+\frac{1}{2}(\sigma_{yy}-p)^2+\frac{1}{2}(\sigma_{zz}-p)^2+\sigma_{xy}^2+\sigma_{xz}^2+\sigma_{yz}^2} \tag{6}$$

and $\dot{\varepsilon}_{\text{dis}}$ as the second invariant of the viscous strain rate for dislocation creep, which is defined as:

$$\dot{\varepsilon}_{\text{dis}}=B_{\text{dis}}A_\varepsilon(\tau_{II})^n\exp\left(-\frac{E_{\text{dis}}}{RT}\right) \tag{7}$$

where $B_{\text{dis}}$ is the material-dependent creep parameter or pre-exponential factor, $A_\varepsilon$ is a strain-dependent function of an arbitrary factor $A$, which we call the weakening amplitude (defined below), $n$ is the power law stress exponent, $E_{\text{dis}}$ the activation enthalpy, and $R$ the gas constant (Popov & Sobolev, 2008). Flow law parameters for Carrara marble and Solnhofen limestone are given in Table 1.

To account for the rheological weakening mechanisms operating in rocks at elevated temperatures and pressures, we implement the function $A_\varepsilon$ that captures progressive weakening. The strain rate $\dot{\varepsilon}_{\text{dis}}$ in each element is increased by this factor $A_\varepsilon$ depending on the actual viscous strain $\varepsilon$ of the element:

$$A_\varepsilon=\begin{cases}1 & \text{if} \quad \varepsilon<\varepsilon_1\\ 1+\dfrac{A-1}{\varepsilon_2-\varepsilon_1}(\varepsilon-\varepsilon_1) & \text{if } \varepsilon_1<\varepsilon<\varepsilon_2\\ A & \text{if} \quad \varepsilon>\varepsilon_2\end{cases} \tag{8}$$

The threshold values $\varepsilon_1$ and $\varepsilon_2$ depend either on (1) accumulated finite viscous strain (see Cyprych et al., 2016) or (2) deformation work per element volume $W_{\text{def}}$ defined as

**Table 1**
*Flow Laws and Boundary Conditions for the Reference Model*

| | Boundary conditions | | Flow laws | | Reference strength (at strain rate $1.9 \times 10^{-4}$ $s^{-1}$) | |
|---|---|---|---|---|---|---|
| Phase | $T$ (°C) | Strain rate ($s^{-1}$) | $n$ | $\log_{10}(B_{dis}^{900})$ ($Pa^{-1}$ $s^{-1}$) | Stress (MPa) | Viscosity (Pa s) |
| Carrara marble (matrix) | 900 | $1.9 \times 10^{-4}$ | 7.6[ac] | −59.59[a] | 22.45 | $5.91 \times 10^{10}$ |
| Solnhofen limestone (inlcusion) | | | 1.4[a] | −13.10[b] | 5.00 | $1.32 \times 10^{10}$ |

*Note*. Temperature dependence is incorporated in the pre-exponential factor, and flow law parameters are valid for given boundary conditions only (Rybacki et al., 2014). Reference strength gives stress and viscosity at the used bulk shear strain rate ($1.9 \times 10^{-4}$ $s^{-1}$).
[a]Rybacki et al. (2014). [b]Rybacki et al. (2014) report −12.55 was modified such that peak stress of model is equivalent to experiment. [c]Schmid et al. (1980).

$$W_{def} = \varepsilon_{visc} \times \tau_{II} \quad (9)$$

with $\varepsilon_{visc}$ as the viscous component of finite strain, which is computed by integrating the second invariant of the deviatoric viscous strain rate tensor with respect to time. For all $\varepsilon < \varepsilon_1$ the factor $A_\varepsilon$ is 1. With increasing finite viscous strain, $A_\varepsilon$ is linearly increased between the threshold values $\varepsilon_1$ and $\varepsilon_2$. For $\varepsilon > \varepsilon_2$, $A_\varepsilon$ is equivalent to the weakening amplitude $A$. As a result, this parameterization reduces the effective viscosity (see Figure 1b). The thresholds $\varepsilon_1$ and $\varepsilon_2$ and the weakening amplitude $A$ of the reference model are determined manually by iterative comparison to experimental observations (Figure 2a). $A$ is chosen such that the stress drop observed from peak stress until the end of the experiment is matched. The threshold values $\varepsilon_1$ and $\varepsilon_2$ control the onset and the end of weakening and were selected such that the shape of the stress strain curve from the experiment is reproduced by the numerical model.

### 3.2. Setup of the Numerical Model

Our reference model is designed to reproduce the single inclusion experiments of Nardini et al. (2018) described above in 2-D Cartesian coordinates. We model the laboratory shear deformation of a hollow cylinder by using periodic boundary conditions, such that material leaving one side of the model in shear direction enters again on the opposite side (see Figure 1c). The model height is 10 mm, and the length of the model along shear direction is 47.124 mm, which represents the outer circumference of the hollow cylinder in the laboratory experiment. Thermal properties of the material do not influence the model results, due to an imposed temperature of 900 °C and the small model size. For the same reason temperature gradients are quickly dissipated, which is why shear heating does not play a role. To compare with the experiments, we apply constant strain rate and constant stress boundary conditions, respectively.

Flow laws implemented in the models are based on a series of torsion and triaxial experiments performed on Carrara marble and Solnhofen limestone by Rybacki et al. (2014). The flow law parameters are similar to those obtained by Schmid et al. (1980). Activation energy and thus temperature dependency are incorporated into the material-dependent pre-exponential parameter ($B_{dis}^{900}$), as the experiments and models are performed at a constant temperature (900 °C; see Table 1). The Solnhofen limestone flows as a superplastic material at the given P-T conditions (Schmid et al., 1977), due to its small grain size. This is incorporated into the model setup by employing a low stress exponent of $n = 1.4$ derived by Rybacki et al. (2014).

## 4. Numerical Model Results

### 4.1. Benchmarking of the Numerical Model

We deduce the three weakening parameters of our strain-dependent softening parametrization ($\varepsilon_1$, $\varepsilon_2$, $A$), by iterative comparison between experiments and model. The experimentally derived stress-strain curve and final strain distribution are successfully reproduced using a model with the following values for the accumulated finite strain thresholds: $\varepsilon_1 = 0.2$, $\varepsilon_2 = 0.5$ and the weakening amplitude: $A = 6$ (Figure 1b) affecting the Carrara marble.

Our model results are in excellent agreement with experimental results at constant strain rate (CTR1). Stress strain curve (see Figure 2a), shear zone width, and matrix deformation are very similar as shown by the passive strain markers (see Figures 2b and 2c). The inclusion length fits to the experimental estimate and its distorted rhomboidal shape (Rybacki et al., 2014) is also observed in the model. Steady state deformation is not yet reached at a bulk shear strain of $\gamma = 1$, indicated by the nonzero slope of the stress strain curve. Constant

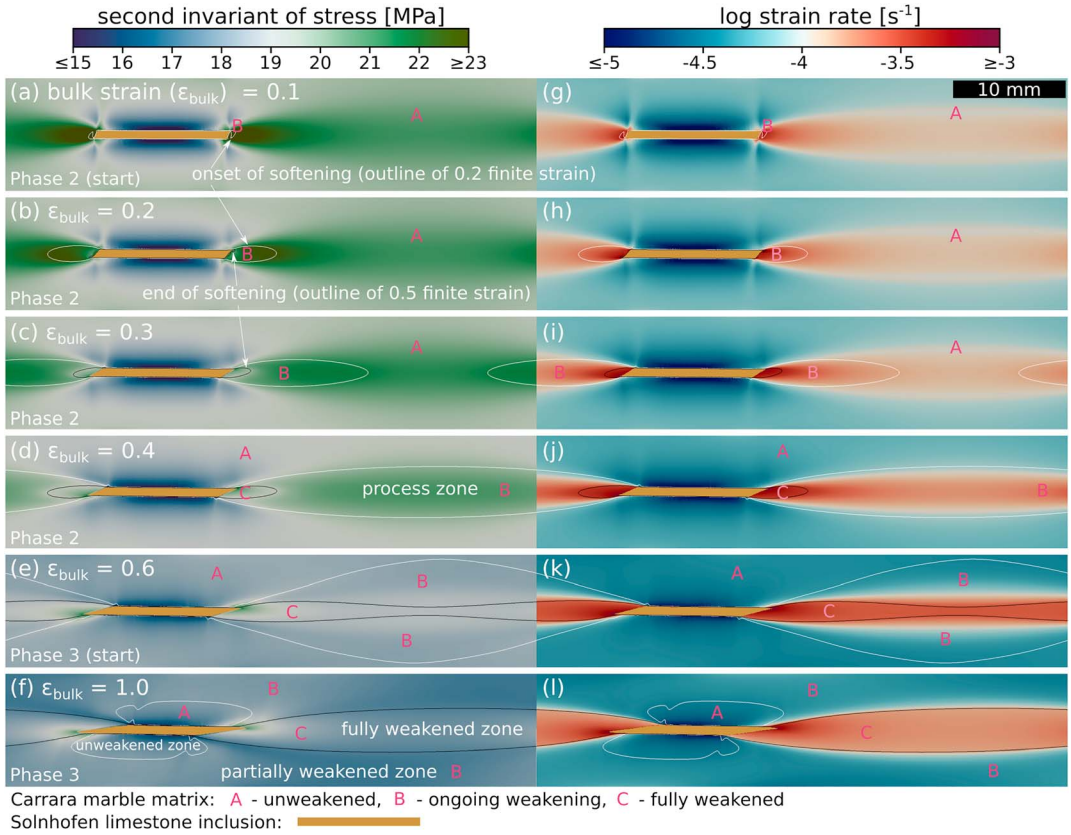


**Figure 3.** Local stress (second invariant of the effective deviatoric stress) (a–f) and strain rate (g–l) evolution within the matrix of the constant strain rate benchmark model. A, B, and C distinguish three different Carrara marble zones and their outlines indicate finite strain thresholds of $\varepsilon_1 = 0.2$ for beginning (white) and $\varepsilon_2 = 0.5$ for end (black) of softening. The process zone B is associated with a local stress maximum propagating into the matrix (a–c). The zone is controlled by the onset and end of softening. A second stress peak remains fixed at the inclusion tips (a–f).

stress model and experimental results also do not differ significantly as shown in the supplements (Figure S1). In agreement with the results from Nardini et al. (2018), this test likewise indicates that both loading configurations (constant strain rate and constant stress) lead to nucleation of ductile shear zones.

The benchmark comparison also reveals a minor difference between model and experiment. When using the experimentally determined flow laws, we find that the maximum bulk shear stress of the model is ~5% lower than in the experiment. Likely, this offset is due to experimental uncertainties contained in the flow laws, which we level out by adopting a slightly smaller pre-exponential factor for the Solnhofen inclusion (Table 1).

### 4.2. Spatial and Temporal Model Evolution

In this section we investigate the bulk stress evolution by analyzing the evolution of model-intrinsic strength variations that arise from the flow laws and local stress partitioning. To describe inhomogeneous deformation surrounding the shear zone tip, we use the term *process zone*, which originates from nonlinear fracture mechanics (Zang et al., 2000). Here we expand its meaning to viscous materials describing a region of enhanced microstructural modification in comparison to the remaining matrix (Rybacki et al., 2014). To analyze the evolution of the process zone that is observed in the experiments, we visualize the stress and strain distribution in space and time. We distinguish four phases (P1–P4) during model evolution: *preweakening* (P1), *onset and acceleration of weakening* (P2), *deceleration of weakening* (P3), and *steady state* (P4). In phase P1 stresses build up (loading) and no material is weakened by viscous softening, but with ongoing deformation the shear strain locally exceeds the threshold strain $\varepsilon_1$ defining the beginning of weakening and phase P2 at a bulk shear strain of $\gamma \sim 0.05$. From this moment on the Carrara marble matrix is subdivided into an unaltered zone A and the process zone B that is submitted to ongoing weakening (Figure 3). With

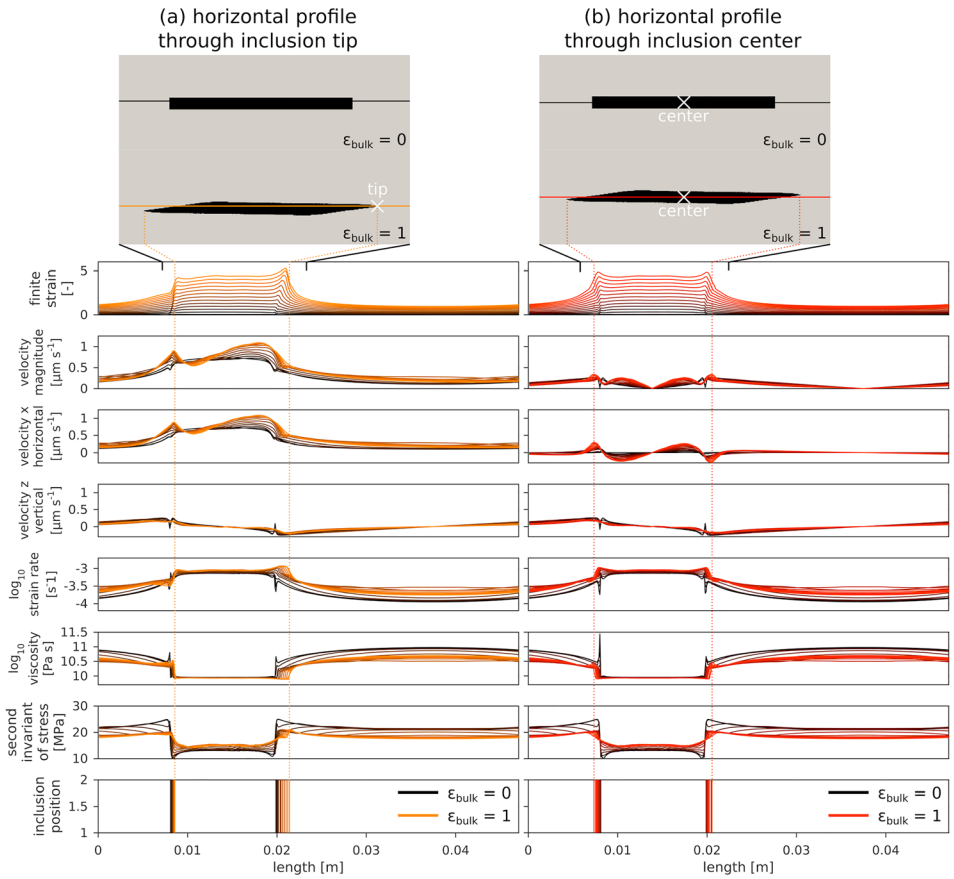


**Figure 4.** Along-strike variations of key variables through time. The inclusion deforms due to simple shear generating differences between horizontal profiles at various vertical positions. Here we show horizontal profiles along the center of the inclusion (at a bulk shear strain of 1) and along the center of overall model domain, which is also the center of the inclusion. (a) Horizontal profile along the center of the inclusion tip. Maximum rate of deformation and accumulated finite strain are found in the inclusion tip and maximum stress in the matrix directly in front of the inclusion tip. (b) Horizontal profile along the model center. Due to the symmetry of the setup, results are approximately point symmetric to the model center.

progressive deformation the process zone grows and a larger volume exceeds the weakening threshold, accelerating bulk softening. At a bulk shear strain of $\gamma \sim 0.6$ the process is slowing down defining the beginning of P3. Two fully weakened regions C emerge in the model center where shear strains start to exceed $\varepsilon_2$ that defines the second threshold and completion of weakening (Figure 3d). In phase P4 the deformation proceeds at steady state, which is only observed for bulk shear strains $\gamma > 2$ using the reference setup. In the experiment and the benchmark model, steady state is not reached since the test is terminated at a bulk shear strain of $\gamma \sim 1$.

Pronounced stress peaks in front of the inclusion tips are observed during early stages of deformation (P1 and early P2; see Figure 3a) resulting in higher strain rates (Figure 3g) than in surrounding matrix regions of low stress. Similar to the experimental results, strain rates in the process zone are locally increased by up to a factor of ~30 in comparison to the matrix. Due to this stress and thus strain rate differences, the finite strain threshold value $\varepsilon_1$ (white outline) is first exceeded at the inclusion tips where softening of the material starts. This leads to a positive feedback promoting localization. Strain rate subsequently increases further and soon the second threshold value $\varepsilon_2$ (black outline) is also exceeded indicating local completion of softening (see Figures 3b–3f and 3h–3l). Consequently, stress gradually decreases again locally between the onset outline and the inclusion (see Figures 3b and 3c). The stress concentrations at the inclusion tips remain due to the remaining viscosity contrast between matrix and inclusion. The cylindrical symmetry of the

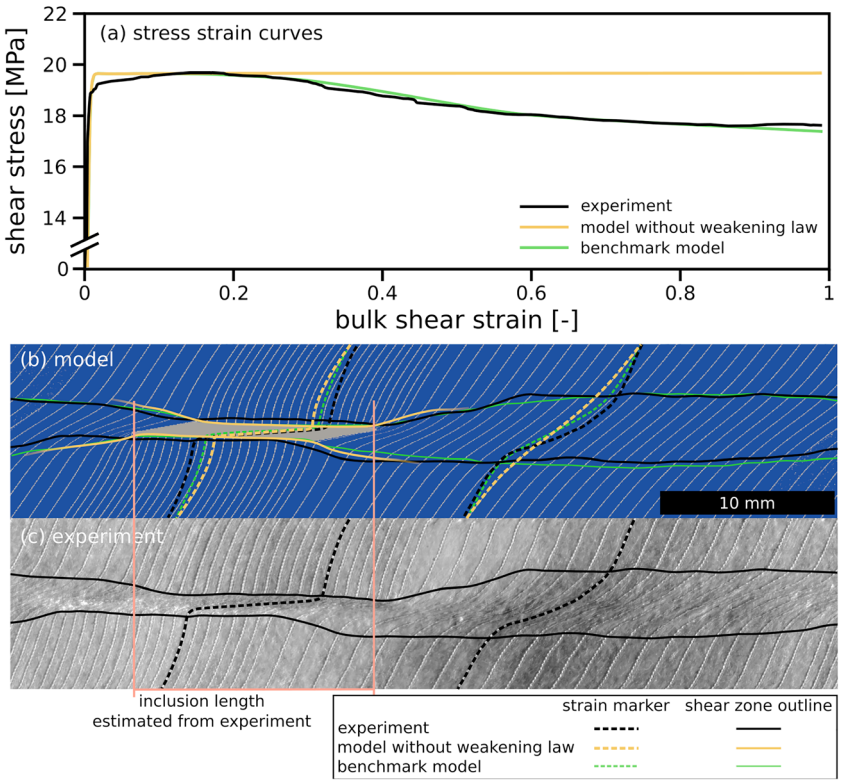


**Figure 5.** Comparison of model without the weakening law to experiment and reference model (same as in Figure 2c). (a) Stress strain curves of model without weakening law (yellow), experiment (black) and reference model (green). (b) Model without weakening law with passive strain markers and shear zone outlines of model where inferable (yellow), experiment (black) and reference model (green). (c) Copper jacket from experiment with passive strain markers, estimated inclusion length and shear zone outline. Results in (b) and (c) are shown at a bulk shear strain of $\gamma \sim 1$. In comparison to the reference model, shear stress remains constant over time and the shear zone in the matrix is less pronounced.

experiment and our model results in a merge of the two weakening fronts ($\varepsilon_1$ outline). Once the two local stress peaks causing the onset of softening merge, they combine to a single, local stress maximum in the model center and the stress gradient in the process zone decreases significantly with further deformation (see Figure 3e). The fully weakened zones C grow, as the process zone B propagates into the matrix from the inclusion, featuring a gradual stress increase from the end of softening outline toward the inclusion tips (see Figure 3d). In phase P3 the completely weakened areas in the vertical model center are connected (see Figures 3e and 3k), after which the rate of weakening decreases (Figure 2a). Stress and strain rates directly above and below the inclusion remain low throughout the experiment due to local stress partitioning. A small transition zone between the inclusion and matrix exists due to coupling of the materials. The overall observed stress drop in the matrix (Figures 3a–3f) results from our weakening parameterization, which decreases the effective viscosity of the Carrara marble.

**Table 2**
*Parameters for Models Used to Test the Effect of the Weakening Amplitude (A) of the Softening Law*

| Models for testing weakening amplitude $A$ | $\varepsilon_1$ | $\varepsilon_2$ | $\Delta_\varepsilon$ | $A$ |
|---|---|---|---|---|
| M0—no softening | — | — | — | 1 |
| M1—reference model | 0.2 | 0.5 | 0.3 | 6 |
| A1 | 0.2 | 0.5 | 0.3 | 20 |
| A2 | 0.2 | 0.5 | 0.3 | 100 |
| A3 | 0.2 | 0.5 | 0.3 | 500 |

Analytical solutions of a linear dislocation in an elastic half-space predict extremely high stresses as displacements vanish toward fracture tips (Okada, 1985). Within the ductile regime and for inclusions of finite width, however, we can show that the localization process at the inclusion tip evolves in a smoother and time-dependent way. Figure 4 shows length profiles that display key parameter values and their evolution with increasing bulk strain along two horizontal model cross sections. The position of profile (a) is chosen such that it crosses the center of the right inclusion tip at a bulk shear strain of 1 which is 0.1 mm above profile (b) along the model center. Horizontal velocity in profile (a) is increased, due to the vertical shift in position.

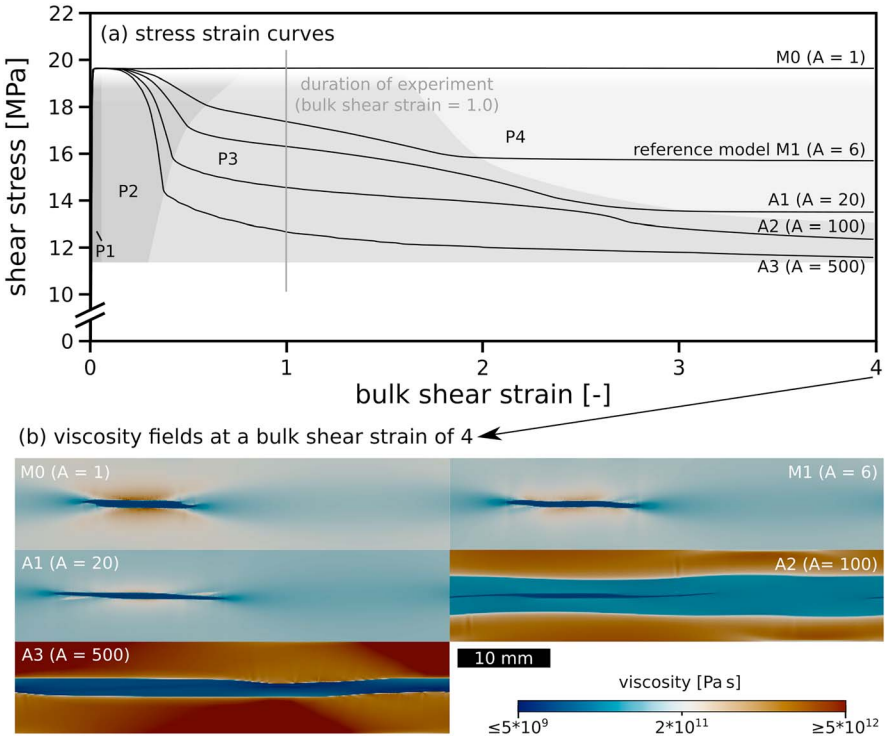


**Figure 6.** Effect of the weakening amplitude $A$. (a) Stress strain curves of models with different weakening amplitude. For comparison the duration of the torsion experiment is indicated. P1–P4 refer to the phases described in chapter 3.4: pre-weakening (P1), onset and acceleration of weakening (P2), deceleration of weakening (P3), and steady state (P4). (b) Viscosity fields of the models at a bulk shear strain of 4. The inclusion in the reference model is elongated further than in the model without weakening, as the matrix is increasingly deformed due to the softening law. This effect increases with $A$. For values of $A > 50$, strain localization is strongly pronounced, as shown by the viscosity field of models with a weakening amplitude $A$ of 100 and 500. Higher values of weakening amplitude lead to stronger weakening and localization.

By that, the point symmetry to the inclusion center is broken, which on the other hand is a feature of profile (b). Similar to a dislocation in an elastic medium, the area surrounding the inclusion tip exhibits high gradients in deformation and stress. The profiles show the highest strain rates and strains inside the weak inclusion directly at the tip. Highest stress values are, however, observed in the matrix in front of the inclusion. Local strain in the process zone at the inclusion tip increases approximately linear with bulk strain by a factor of ~4.

### 4.3. The Impact of Softening on the Reference Model

To better constrain the effect of the viscous softening formalism, we run an additional constant strain rate model, but without the strain dependent weakening law. Besides the differences in the stress strain curves (Figure 5a), also a less pronounced shear zone development is observed (Figure 5b). This is indicated by the linearly deflected, yellow strain marker crossing the matrix and the yellow shear zone outline. Strain is instead localizing mainly in the inclusion and, to a lesser extent, in the matrix close to the inclusion tips. Nonetheless, the results of this test still show reasonable agreement with the experimental data, because the bulk weakening is generally low for the used samples and setup, which is indicated by the total shear stress drop of just ~2 MPa in the experiment.

Additionally, we test a softening law that is based on deformation work instead of finite strain as discussed above. In this formulation, the weakening thresholds ($\varepsilon_1$ and $\varepsilon_2$, equation (8)) are not based on

**Table 3**
*Parameters for Models Used to Test the Effect of Onset ($\varepsilon_1$) and end ($\varepsilon_2$) of the Softening Law*

| Models for testing onset and end | $\varepsilon_1$ | $\varepsilon_2$ | $\Delta_\varepsilon$ | $A$ |
|---|---|---|---|---|
| M0—no softening | — | — | — | 1 |
| M1—reference model | 0.2 | 0.5 | 0.3 | 6 |
| E1 | 0.0 | 0.5 | 0.5 | 6 |
| E2 | 0.2 | 1.0 | 0.8 | 6 |
| E3 | 0.5 | 1.0 | 0.5 | 6 |

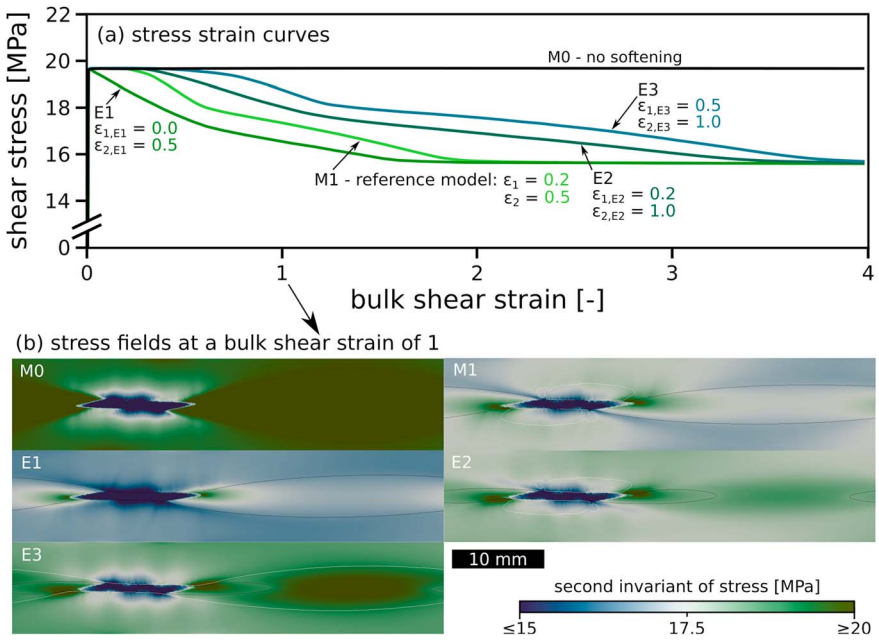


**Figure 7.** Effect of onset and end of weakening on the stress strain evolution. (a) Stress strain curves of models with varying onset ($\varepsilon_1$) and end parameters ($\varepsilon_2$). Note the shapes of curves E1 and E3 (same $\Delta\varepsilon$) indicating a nonlinear relationship between threshold parameters and weakening behavior. (b) Stress field (second invariant of the effective deviatoric stress) of models at bulk shear strain of 1. M0) no softening; M1) reference model; E1) $\varepsilon_1 = 0$; E2) $\varepsilon_2 = 1$; E3) $\varepsilon_1 = 0.5$, and $\varepsilon_2 = 1.0$. Models with lower $\varepsilon_1$ have lower bulk strengths at the same bulk shear strain.

finite strain, but on deformation work as defined in equation (9). Threshold values $\varepsilon_1$ and $\varepsilon_2$ were chosen following the iterative procedure described above for finite strain. However, we find no significant difference to the strain based softening implementation (see supporting information Figure S2).

### 4.4. The Softening Law Parameters

This chapter addresses the effects of the softening law parameters on the localization process. We therefore vary the three controlling parameters (Figure 1b), the finite strain threshold values onset ($\varepsilon_1$) and end ($\varepsilon_2$), and the weakening amplitude ($A$). In order to test the effect of varying $A$, we change this parameter between 1 and 500 leaving the remaining reference model parameters unchanged, that is, $\varepsilon_1$ (0.2) and $\varepsilon_2$ (0.5) (Table 2). Models are conducted up to a bulk shear strain of $\gamma \sim 4$, where steady state conditions are reached in almost all cases. The reference model for instance reaches steady state at a bulk shear strain of approximately 2 (Figure 6a). Increasing $A$ amplifies the weakening of the Carrara marble matrix, resulting in a bulk shear stress drop and enhanced strain and thus shear zone localization, which is also indicated by a decreasing angle between inclusion and matrix shear zone (Figure 6). Large values of $A$ increase the rate of strain localization. This is indicated by the sudden shear stress drop at a bulk shear strain of 0.4 and by faster stress peak propagation into the matrix. For values of $A > 50$ the matrix separates into two zones of substantial viscosity contrast (Figure 6b).

In another experiment, models are run up to a bulk shear strain of 4, varying $\varepsilon_1$and $\varepsilon_2$ at constant $A$ (Table 3). As expected, this shifts the onset and end of weakening—earlier for lower finite shear strain values and later for higher—but the actual effect on the model is not linear (Figure 7a). Note that by changing the strain range of softening $\Delta\varepsilon = \varepsilon_1 - \varepsilon_2$, the slope of the stress strain curve and thus localization rate is affected as well. The reference model with the lowest $\Delta\varepsilon$ displays the fastest localization rate, because the rate with which the pre-exponential factor is increased is higher between the two thresholds due to the linear nature of the softening law. Model E2 with $\Delta\varepsilon$ of 0.8, however, reaches steady state only after a long period of ongoing softening (between 0.4 and 3.4 bulk shear strain). The local stress patterns of the tested models differ at a bulk shear strain of 1, depending on the applied threshold values. While model M0 is in the

preweakening phase P1, model E3 and E2 are in phase P2 and model M1 and E1 already reached phase P3 approaching steady state conditions (Figure 7b).

### 4.5. Ultramylonite Model—The Effect of Progressive Softening and Switch of Deformation Mechanism

Mylonitic shear zones often feature millimeter-centimeter-wide bands with fine grain sizes referred to as ultramylonites (Hippertt & Hongn, 1998; Kenkmann & Dresen, 2002). It is commonly assumed that grain size refinement from cataclasis (Blenkinsop, 1991), dynamic recrystallization (Warren & Hirth, 2006), or mineral reactions (Herwegh et al., 2003) promotes a switch to grain size-sensitive deformation (Bürgmann & Dresen, 2008; Heitzmann, 1987). The switch to grain size-sensitive creep is transient unless grain growth is suppressed (e.g., Pearce et al., 2011), which can be achieved for example by pinning through phase mixing. In order to mimic a progressive change in mechanism, a second softening step is introduced using a similar approach as described above for the onset of weakening (equation (8)), where we add additional strain thresholds for onset ($\varepsilon_3$) and end of weakening ($\varepsilon_4$). This second softening step is exploratory and not based any data. Configuration of the model setup and the initial onset of softening are identical to the reference model; hence, earliest stages of model evolution are the same as before. The introduction of a second softening step with progressive strain, however, is expected to lead to further localization and formation of a narrow low-viscosity layer embedded in the primary shear zone. To this end, finite strain thresholds for onset of weakening ($\varepsilon_3 = 1$) and completion ($\varepsilon_4 = 2$) are chosen, respectively. This procedure enables formation of a localized *ultramylonite* band inside the active shear zone. A high weakening amplitude ($A_{um} = 20$) is chosen to enable fast and strong localization once the threshold $\varepsilon_3$ is reached.

Evolution of the model is equivalent to the reference model for bulk shear strains less than 0.4 (compare Figures 3a–3d to Figures 8a–8d). Upon onset of the second softening stage, strain localizes into a narrow zone in the model center (Figures 8n and 8o). Inside this high strain zone, the inclusion is strongly elongated and an anastomosing pattern of the second shear zone establishes (Figures 8q and 8r) that additionally becomes wider with increasing bulk strain (Figures 8o–8r). This transition to an anastomosing shape forms due to a rotation, which is caused by the shear deformation that the material is subjected to. Despite the simplicity of our setup with a single inclusion, our model nevertheless captures the nested structure and the anastomosing shape of the resulting high-strain band. This agrees very well with common observations of ultramylonite bands in nature (Heitzmann, 1987; Kilian et al., 2011).

## 5. Discussion

### 5.1. Strain Localization and Shear Zone Evolution

The ductile shear zone formation observed in the experiments involves strain localization, rheological weakening of the Carrara marble and bulk strength reduction. Our numerical model reproduces these observations by employing a strain dependent viscous softening law. The model reaches steady state at a bulk shear strain of ~2 in good agreement with observations from experiments (Rybacki et al., 2014). Once steady state is reached, grain size reduction through dynamic recrystallization and grain growth are anticipated to reach a dynamic balance (De Bresser et al., 2001), resulting in steady state material strength. Our model results provide insight into the development of local stress, strain partitioning between matrix, inclusion, and shear zone and ensuing viscosities. This provides detailed insight in the evolution of a localized shear zone that allows a direct comparison with the bulk mechanical data and microstructural observations collected from the deformation experiments. It has to be kept in mind though that the numerical model does not feature the grain-scale resolution necessary to reproduce the brittle deformation as observed in the experiments. Nevertheless, the model successfully predicts local stress concentration and strain rate amplification ahead of the inclusion in first order agreement with the experimental results. This provides confidence to the results of the parameter study performed here, as to the magnitude of softening. This holds in particular to the results of models predicting progressive multistage softening combined with a change in deformation mechanisms, as suggested from a large number of field studies.

The nucleation of a localized shear zone at the inclusion tips involves formation of a process zone. This process zone is defined by a strong local stress concentration and resulting volume of enhanced microstructural modification (Rybacki et al., 2014). In our models this zone is represented by a 2-D area showing local stress

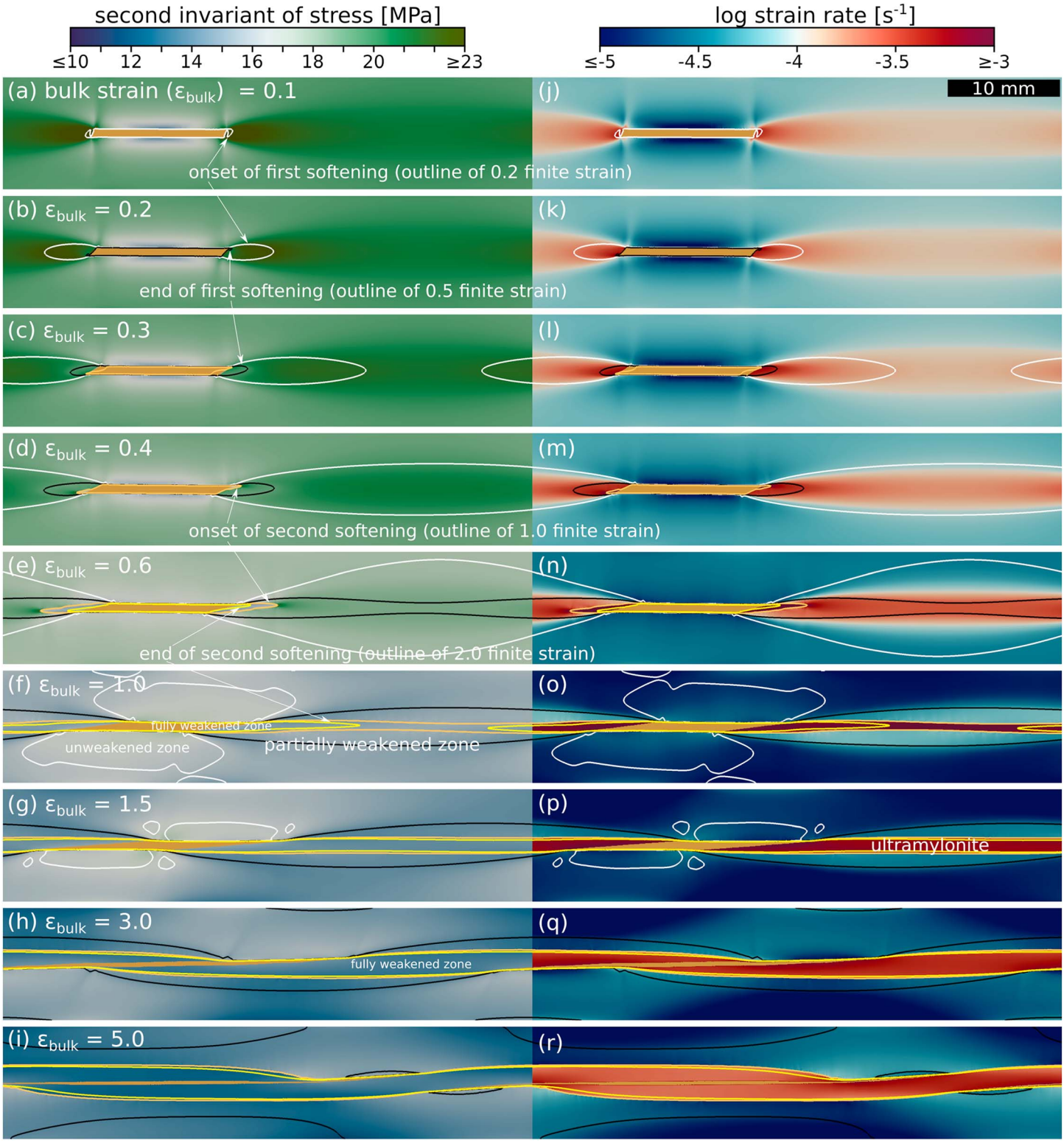


**Figure 8.** Local stress (second invariant of the effective deviatoric stress) (a–i) and strain rate (j–r) evolution within the matrix of the ultramylonite model. Outlines indicate finite strain thresholds $\varepsilon_1 = 0.2$ for onset of softening (white), $\varepsilon_2 = 0.5$ end of first softening stage (black), $\varepsilon_3 = 1.0$ for beginning of second stage (orange), and $\varepsilon_4 = 2.0$ for end of second (yellow) softening stage. The onset of the second softening stage triggers evolution of further localized high strain layer (e, f, n, and o) representing ultramylonite formation within a mylonite.

concentrations that result from the viscosity contrast between limestone and marble present at the assumed temperature conditions. The enhanced stress levels locally reduce the effective viscosity of the Carrara marble (power law rheology) resulting in locally increased strain rates. In turn, this triggers rheological weakening causing shear strain to progressively localize in a shear zone embedded in the Carrara matrix. A localized, elliptical process zone is established, corresponding to the experiments, that displays a zone of gradually reduced grain sizes around the inclusion tips.

### 5.2. Relating our Softening Parameterization to Nature

The two threshold values for finite strain ($\varepsilon_1$ and $\varepsilon_2$) used in the numerical model are expected to mimic the effects that microstructural changes within the process zone have on the bulk strength of the experimentally deformed samples. As such, they are unlikely to represent specific and observable stages of the local microstructural evolution within the process zone. Strain weakening behavior is known to results from a number of different processes, for example, dynamic recrystallization, dislocation annihilation, vacancy diffusion, or lattice preferred orientation. These concur to produce the microstructural and textural modifications that can be observed in our experimental samples in proportions that are likely to vary in the course of the transient processes discussed here. A simple linear parametrization cannot be expected to capture single elements of such complexity within heterogeneously deforming samples. Our parameterization, however, appears to reproduce the phenomenological aspects of weakening as observed in our experiments with reasonably high accuracy.

While it is beyond the scope of our model to pinpoint the micromechanical processes and features corresponding to specific values of local shear strain, some general observations can be made to discuss the significance of our approach. Plastic yield of the bulk assembly, suggesting the onset of strain weakening processes at the local scale, is already observed at very low values of bulk shear strain (~0.01–0.02, cf. Figure 4 in Nardini et al., 2018) corresponding to a local strain of ~0.1–0.2 at the tip of the inclusion (cf. Figure 6a in Nardini et al., 2018), which is in the range of our selected $\varepsilon_1$. It is important to notice that the process zone forming along the weak inclusion plane is intrinsically transient both on a temporal and spatial level. The heterogeneity-induced viscosity contrast produces a volume of stress enhancement (e.g., Figure 3), which evolves with bulk shear strain and determines a strongly heterogeneous strain distribution (Figure 6 in Nardini et al., 2018). Similarly to what would be expected in the brittle regime for slip-weakening behavior, an area of strength perturbation is developed. It is characterized by higher strain rates and increasing microstructural changes closer to the inclusion: the extent of such a perturbation may determine the value of $\varepsilon_2$, that is, the *end of weakening* in our softening law. Whether or not, in a nonsteady state shear zone like is the case in our experimental samples, a microstructural and/or textural signature would be associated at all times with the varying volume of perturbed material is questionable. It is therefore reasonable to conclude that while a definite one-to-one correlation between the described finite strain threshold values and specific microstructural changes is not possible, these parameters are still able to capture the bulk mechanical expression of the strain weakening processes locally activated in the microstructures.

### 5.3. Scope and Limitation of Strain Softening Parametrization

The advantage of employing a simple, first-order softening law is to keep numerical complexity low, which not only is more transparent but also saves computational time in large-scale models (e.g., Brune et al., 2014; Huismans & Beaumont, 2003). In an attempt to model rock weakening and strain localization, different types of softening parameterizations have been previously used in order to describe the weakening behavior of natural materials. For example, Gardner et al. (2017) studied strain localization using different load bearing framework geometries. They found that interconnected weak layers are hard to form without a dynamic weakening process, which was also observed in an experimental study by Holyoke and Tullis (2006). This agrees with our results showing that pronounced shear zone formation in the matrix only occurs for materials with an implemented weakening formalism simulating progressive material softening. This implies the necessity of using softening laws to properly model strain localization and thus shear zone formation. Gardner et al. (2017) used a different implementation to simulate weakening. They introduced stress dependent softening combined with time dependent hardening focusing on the transition from nonlinear to linear flow. At larger scale, Mazzotti and Gueydan (2018) pointed out the fundamental role of inherited tectonic structures for strain and seismicity concentrations in an intraplate setting. Similar to our study, their model also includes irreversible softening (no counteracting hardening mechanism). However, in their model

softening is achieved by changing the material yield stress instead of the pre-exponential factor in a constitutive law, as in this study.

In large-scale rock deformation, there are several major effects that may play an important role affecting localization and shear zone formation and that need to be considered in numerical modeling studies. These are highly nonlinear processes such as shear heating (Duretz et al., 2015; Foley, 2018; Thielmann & Kaus, 2012), melting (Dannberg & Heister, 2016; Schmeling et al., 2018), or a switch to grain size sensitive diffusion creep, like modeled in our study (e.g., Handy, 1989). In that aspect, our models provide a minimum constraint to the degree of viscous strain softening that can be expected to act in nature. Another important point is that numerical models of brittle deformation often involve a strong mesh dependency (De Borst & Mühlhaus, 1992) such that the softening parameters have to be adopted to the chosen resolution. However, this is not the case when modeling viscous deformation where the size of the process zone as well as the bulk shear stress evolution and employed softening parameters ($\varepsilon_1$, $\varepsilon_2$, and $A$) are almost independent of the model resolution.

## 6. Conclusions

Strain localization in shear zones is an important process in lithosphere dynamics occurring over a broad range of spatial scales. For simplicity, we use a piecewise linear softening law and show that it is capable of reproducing rheological weakening observed in laboratory experiments. Our model provides a virtual way of analyzing the viscous process zone evolution that can be divided into four phases (P1) *preweakening*, (P2) *onset and acceleration of weakening*, (P3) *deceleration of weakening*, and (P4) *steady state*. Spatial stress distributions show that matrix strain localization is initiated by a local stress peak at the inclusion tips. From there and with increasing strain, the process zone expands into the matrix. Shear zone width and localization rate are controlled by the amount of rheological weakening. Our numerical models show that rheological weakening is necessary to establish a pronounced shear zone in a strong matrix surrounding a weak inclusion and to explain the anastomosing shape and the nested structure of ultramylonites. This reinforces the importance for geodynamic models to contain softening laws that appropriately account for rheological weakening.

**Acknowledgments**
This manuscript has been greatly improved thanks to the constructive comments and suggestions of Andrew Cross, an anonymous reviewer, and associate editor Bjarne Almqvist. This study was conducted within the Helmholtz Young Investigators Group CRYSTALS (VH-NG-1132). Laboratory experiments were performed in Geomechanics and Rheology section of the German Research Centre for Geosciences, and we thank Stefan Gehrmann for help with sample preparation. Simulations were performed on the cluster facilities of the German Research Centre for Geosciences. All data that this numerical study is based on are found in Figure 1 and the parameter Tables 1, 2, and 3. Additional data regarding the torsion experiment are found within Nardini et al. (2018). Figures were created using Paraview and Matlab and color maps were taken from Crameri (2018).

## References

Ballato, P., Brune, S., & Strecker, M. R. (2019). Sedimentary loading–unloading cycles and faulting in intermontane basins: Insights from numerical modeling and field observations in the NW Argentine Andes. *Earth and Planetary Science Letters*, *506*, 388–396. https://doi.org/10.1016/j.epsl.2018.10.043

Barnhoorn, A., Bystricky, M., Burlini, L., & Kunze, K. (2004). The role of recrystallisation on the deformation behaviour of calcite rocks: Large strain torsion experiments on Carrara marble. *Journal of Structural Geology*, *26*(5), 885–903. https://doi.org/10.1016/j.jsg.2003.11.024

Bercovici, D., & Ricard, Y. (2012). Generation of plate tectonics with two-phase grain-damage and pinning. *Physics of the Earth and Planetary Interiors*, *202*, 27–55. https://doi.org/10.1016/j.pepi.2012.05.003

Blenkinsop, T. G. (1991). Cataclasis and processes of particle size reduction. *Pure and Applied Geophysics*, *136*(1), 59–86. https://doi.org/10.1007/BF00878888

Bonet, J., & Wood, R. D. (1997). *Nonlinear continuum mechanics for finite element analysis*. New York: Cambridge University Press. https://doi.org/10.1017/CBO9780511755446

Bruhn, D. F., & Casey, M. (1997). Texture development in experimentally deformed two-phase aggregates of calcite and anhydrite. *Journal of Structural Geology*, *19*(7), 909–925. https://doi.org/10.1016/S0191-8141(97)00023-0

Bruhn, D. F., Olgaard, D. L., & Dell'Angelo, L. N. (1999). Evidence for enhanced deformation in two-phase rocks: Experiments on the rheology of calcite-anhydrite aggregates. *Journal of Geophysical Research*, *104*, 707–724. https://doi.org/10.1029/98JB02847

Brune, S. (2014). Evolution of stress and fault patterns in oblique rift systems: 3-D numerical lithospheric-scale experiments from rift to breakup. *Geochemistry, Geophysics, Geosystems*, *15*, 3392–3415. https://doi.org/10.1002/2014GC005446

Brune, S., & Autin, J. (2013). The rift to break-up evolution of the Gulf of Aden: Insights from 3D numerical lithospheric-scale modelling. *Tectonophysics*, *607*, 65–79. https://doi.org/10.1016/j.tecto.2013.06.029

Brune, S., Heine, C., Clift, P. D., & Pérez-Gussinyé, M. (2017). Rifted margin architecture and crustal rheology: Reviewing Iberia-Newfoundland, Central South Atlantic, and South China Sea. *Marine and Petroleum Geology*, *79*, 257–281. https://doi.org/10.1016/j.marpetgeo.2016.10.018

Brune, S., Heine, C., Pérez-Gussinyé, M., & Sobolev, S. V. (2014). Rift migration explains continental margin asymmetry and crustal hyperextension. *Nature Communications*, *5*(1), 4014. https://doi.org/10.1038/ncomms5014

Brune, S., Popov, A. A., & Sobolev, S. V. (2012). Modeling suggests that oblique extension facilitates rifting and continental break-up. *Journal of Geophysical Research*, *117*, B08402. https://doi.org/10.1029/2011JB008860

Brune, S., Popov, A. A., & Sobolev, S. V. (2013). Quantifying the thermo-mechanical impact of plume arrival on continental break-up. *Tectonophysics*, *604*, 51–59. https://doi.org/10.1016/j.tecto.2013.02.009

Brune, S., Williams, S. E., Butterworth, N. P., & Müller, R. D. (2016). Abrupt plate accelerations shape rifted continental margins. *Nature*, *536*(7615), 201–204. https://doi.org/10.1038/nature18319

Bürgmann, R., & Dresen, G. (2008). Rheology of the lower crust and upper mantle: Evidence from rock mechanics, geodesy, and field observations. *Annual Review of Earth and Planetary Sciences*, *36*(1), 531–567. https://doi.org/10.1146/annurev.earth.36.031207.124326

Burlini, L., & Bruhn, D. (2005). High-strain zones: Laboratory perspectives on strain softening during ductile deformation. *Geological Society, London, Special Publications*, *122*(10), 7584–7596. https://doi.org/10.1002/2017JB014333

Clift, P. D., Brune, S., & Quinteros, J. (2015). Climate changes control offshore crustal structure at South China Sea continental margin. *Earth and Planetary Science Letters*, *420*, 66–72. https://doi.org/10.1016/j.epsl.2015.03.032

Cook, A. C., Vel, S. S., Gerbi, C., & Johnson, S. E. (2014). Computational analysis of nonlinear creep of polyphase aggregates: Influence of phase morphology. *Journal of Geophysical Research, B: Solid Earth*, *119*, 6877–6906. https://doi.org/10.1002/2014JB011197

Corti, G., van Wijk, J., Cloetingh, S., & Morley, C. K. (2007). Tectonic inheritance and continental rift architecture: Numerical and analogue models of the East African Rift system. *Tectonics*, *26*, TC6006. https://doi.org/10.1029/2006TC002086

Coyan, M. M., Arrowsmith, J. R., Umhoefer, P., Coyan, J., Kent, G., Driscoll, N., & Gutíerrez, G. M. (2013). Geometry and quaternary slip behavior of the San Juan de los Planes and Saltito fault zones, Baja California Sur, Mexico: Characterization of rift-margin normal faults. *Geosphere*, *9*(3), 426–443. https://doi.org/10.1130/GES00806.1

Crameri, F. (2018). Geodynamic diagnostics, scientific visualisation and StagLab 3.0. *Geoscientific Model Development Discussion*, 1–41. https://doi.org/10.5194/gmd-2017-328

Cross, A. J., Ellis, S., & Prior, D. J. (2015). A phenomenological numerical approach for investigating grain size evolution in ductiley deforming rocks. *Journal of Structural Geology*, *76*, 22–34. https://doi.org/10.1016/j.jsg.2015.04.001

Cross, A. J., & Skemer, P. (2017). Ultramylonite generation via phase mixing in high-strain experiments. *Journal of Geophysical Research: Solid Earth*, *122*, 1744–1759. https://doi.org/10.1002/2016JB013801

Cyprych, D., Brune, S., Piazolo, S., & Quinteros, J. (2016). Strain localization in polycrystalline material with second phase particles: Numerical modeling with application to ice mixtures. *Geochemistry, Geophysics, Geosystems*, *17*, 3608–3628. https://doi.org/10.1002/2016GC006471

Dannberg, J., & Heister, T. (2016). Compressible magma/mantle dynamics: 3-D, adaptive simulations in ASPECT. *Geophysical Journal International*, *207*(3), 1343–1366. https://doi.org/10.1093/gji/ggw329

De Borst, R., & Mühlhaus, H. B. (1992). Gradient-dependent plasticity: Formulation and algorithmic aspects. *International Journal for Numerical Methods in Engineering*, *35*(3), 521–539. https://doi.org/10.1002/nme.1620350307

De Bresser, J. H. P., Ter Heege, J. H., & Spiers, C. J. (2001). Grain size reduction by dynamic recrystallization: Can it result in major rheological weakening? *International Journal of Earth Sciences*, *90*(1), 28–45. https://doi.org/10.1007/s005310000149

Dimanov, A., & Dresen, G. (2005). Rheology of synthetic anorthite-diopside aggregates: Implications for ductile shear zones. *Journal of Geophysical Research*, *110*, B07203. https://doi.org/10.1029/2004JB003431

Duesterhoeft, E., Quinteros, J., Oberhänsli, R., Bousquet, R., & de Capitani, C. (2014). Relative impact of mantle densification and eclogitization of slabs on subduction dynamics: A numerical thermodynamic/thermokinematic investigation of metamorphic density evolution. *Tectonophysics*, *637*, 20–29. https://doi.org/10.1016/j.tecto.2014.09.009

Duretz, T., Petri, B., Mohn, G., Schmalholz, S. M., Schenker, F. L., & Müntener, O. (2016). The importance of structural softening for the evolution and architecture of passive margins. *Scientific Reports*, *6*(1). https://doi.org/10.1038/srep38704

Duretz, T., Schmalholz, S. M., & Podladchikov, Y. Y. (2015). Shear heating-induced strain localization across the scales. *Philosophical Magazine*, *95*(28–30), 3192–3207. https://doi.org/10.1080/14786435.2015.1054327

Foley, B. J. (2018). On the dynamics of coupled grain size evolution and shear heating in lithospheric shear zones. *Physics of the Earth and Planetary Interiors*, *283*, 7–25. https://doi.org/10.1016/j.pepi.2018.07.008

Fossen, H., & Cavalcante, G. C. G. (2017). Shear zones—A review. *Earth-Science Reviews*, *171*, 434–455. https://doi.org/10.1016/j.earscirev.2017.05.002

Gardner, R., Piazolo, S., Evans, L., & Daczko, N. (2017). Patterns of strain localization in heterogeneous, polycrystalline rocks—A numerical perspective. *Earth and Planetary Science Letters*, *463*, 253–265. https://doi.org/10.1016/j.epsl.2017.01.039

Gerbi, C., Johnson, S. E., Cook, A., & Vel, S. S. (2015). Effect of phase morphology on bulk strength for power-law materials. *Geophysical Journal International*, *200*(1), 374–389. https://doi.org/10.1093/gji/ggu388

Handy, M. R. (1989). Deformation regimes and the rheological evolution of fault zones in the lithosphere: The effects of pressure, temperature, grainsize and time. *Tectonophysics*, *163*(1-2), 119–152. https://doi.org/10.1016/0040-1951(89)90122-4

Handy, M. R., Mulch, A., Rosenau, M., & Rosenberg, C. L. (2001). The role of fault zones and melts as agents of weakening, hardening and differentiation of the continental crust: A synthesis. *Geological Society, London, Special Publications*, *186*(1), 305–332. https://doi.org/10.1144/GSL.SP.2001.186.01.18

Heine, C., & Brune, S. (2014). Oblique rifting of the equatorial Atlantic: Why there is no saharan Atlantic Ocean. *Geology*, *42*(3), 211–214. https://doi.org/10.1130/G35082.1

Heitzmann, P. (1987). Calcite mylonites in the central root zone. *Tectonophysics*, *135*(1–3), 207–215. https://doi.org/10.1016/0040-1951(87)90162-4

Herwegh, M., Berger, A., & Ebert, A. (2005). Grain coarsening maps: A new tool to predict microfabric evolution of polymineralic rocks. *Geology*, *33*(10), 801–804. https://doi.org/10.1130/G21789.1

Herwegh, M., Poulet, T., Karrech, A., & Regenauer-Lieb, K. (2014). From transient to steady state deformation and grain size: A thermodynamic approach using elasto-visco-plastic numerical modeling. *Journal of Geophysical Research: Solid Earth*, *119*, 900–918. https://doi.org/10.1002/2013JB010701

Herwegh, M., Xiao, X., & Evans, B. (2003). The effect of dissolved magnesium on diffusion creep in calcite. *Earth and Planetary Science Letters*, *212*(3–4), 457–470. https://doi.org/10.1016/S0012-821X(03)00284-X

Hippertt, J. F., & Hongn, F. D. (1998). Deformation mechanisms in the mylonite/ultramylonite transition. *Journal of Structural Geology*, *20*(11), 1435–1448. https://doi.org/10.1016/S0191-8141(98)00047-9

Holyoke, C. W., & Tullis, J. (2006). Mechanisms of weak phase interconnection and the effects of phase strength contrast on fabric development. *Journal of Structural Geology*, *28*(4), 621–640. https://doi.org/10.1016/j.jsg.2006.01.008

Huismans, R. S., & Beaumont, C. (2003). Symmetric and asymmetric lithospheric extension: Relative effects of frictional-plastic and viscous strain softening. *Journal of Geophysical Research*, *108*(B10), 2496. https://doi.org/10.1029/2002JB002026

Jammes, S., Lavier, L. L., & Reber, J. E. (2015). Localization and delocalization of deformation in a bimineralic material. *Journal of Geophysical Research: Solid Earth*, *120*, 3649–3663. https://doi.org/10.1002/2015JB011890

Jessell, M. W., Siebert, E., Bons, P. D., Evans, L., & Piazolo, S. (2005). A new type of numerical experiment on the spatial and temporal patterns of localization of deformation in a material with a coupling of grain size and rheology. *Earth and Planetary Science Letters*, *239*(3–4), 309–326. https://doi.org/10.1016/j.epsl.2005.03.030

Ji, S., Jiang, Z., Rybacki, E., Wirth, R., Prior, D., & Xia, B. (2004). Strain softening and microstructural evolution of anorthite aggregates and quartz-anorthite layered composites deformed in torsion. *Earth and Planetary Science Letters*, *222*(2), 377–390. https://doi.org/10.1016/j.epsl.2004.03.021

Kenkmann, T., & Dresen, G. (1998). Stress gradients around porphyroclasts: Palaeopiezometric estimates and numerical modelling. *Journal of Structural Geology*, *20*(2-3), 163–173. https://doi.org/10.1016/S0191-8141(97)00074-6

Kenkmann, T., & Dresen, G. (2002). Dislocation microstructure and phase distribution in a lower crustal shear zone—An example from the Ivrea-Zone, Italy. *International Journal of Earth Sciences*, *91*(3), 445–458. https://doi.org/10.1007/s00531-001-0236-9

Kilian, R., Heilbronner, R., & Stünitz, H. (2011). Quartz grain size reduction in a granitoid rock and the transition from dislocation to diffusion creep. *Journal of Structural Geology*, *33*(8), 1265–1284. https://doi.org/10.1016/j.jsg.2011.05.004

Koopmann, H., Brune, S., Franke, D., & Breuer, S. (2014). Linking rift propagation barriers to excess magmatism at volcanic rifted margins. *Geology*, *42*(12), 1071–1074. https://doi.org/10.1130/G36085.1

Linckens, J., Herwegh, M., Mntener, O., & Mercolli, I. (2011). Evolution of a polymineralic mantle shear zone and the role of second phases in the localization of deformation. *Journal of Geophysical Research*, *116*, B06210. https://doi.org/10.1029/2010JB008119

Mancktelow, N. S. (2002). Finite-element modelling of shear zone development in viscoelastic materials and its implications for localisation of partial melting. *Journal of Structural Geology*, *24*(6–7), 1045–1053. https://doi.org/10.1016/S0191-8141(01)00090-6

Mancktelow, N. S., & Pennacchioni, G. (2005). The control of precursor brittle fracture and fluid-rock interaction on the development of single and paired ductile shear zones. *Journal of Structural Geology*, *27*(4), 645–661. https://doi.org/10.1016/j.jsg.2004.12.001

Mazzotti, S., & Gueydan, F. (2018). Control of tectonic inheritance on continental intraplate strain rate and seismicity. *Tectonophysics*, *746*, 602–610. https://doi.org/10.1016/j.tecto.2017.12.014

Misra, S., & Mandal, N. (2007). Localization of plastic zones in rocks around rigid inclusions: Insights from experimental and theoretical models. *Journal of Geophysical Research*, *112*, B09206. https://doi.org/10.1029/2006JB004328

Nardini, L., Rybacki, E., Döhmann, M. J. E. A., Morales, L. F., Brune, S., & Dresen, G. (2018). High-temperature shear zone formation in Carrara marble: The effect of loading conditions. *Tectonophysics*, *749*, 120–139. https://doi.org/10.1016/j.tecto.2018.10.022

Okada, Y. (1985). Surface deformation due to shear and tensile faults in a half-space. *Bulletin of the Seismological Society of America*, *75*(4), 1135–1154.

Palin, R. M., Searle, M. P., St-Onge, M. R., Waters, D. J., Roberts, N. M. W., Horstwood, M. S. A., et al. (2014). Two-stage cooling history of pelitic and semi-pelitic mylonite (sensu lato) from the Dongjiu-Milin shear zone, northwest flank of the eastern Himalayan syntaxis. *Gondwana Research*, *28*(2), 509–530. https://doi.org/10.1016/j.gr.2014.07.009

Park, M., & Jung, H. (2017). Microstructural evolution of the Yugu peridotites in the Gyeonggi Massif, Korea: Implications for olivine fabric transition in mantle shear zones. *Tectonophysics*, *709*, 55–68. https://doi.org/10.1016/j.tecto.2017.04.017

Paterson, M. S. (1970). A high-pressure, high-temperature apparatus for rock deformation. *International Journal of Rock Mechanics and Mining Sciences*, *7*(5), 517–526. https://doi.org/10.1016/0148-9062(70)90004-5

Paterson, M. S., & Olgaard, D. L. (2000). Rock deformation tests to large shear strains in torsion. *Journal of Structural Geology*, *22*(9), 1341–1358. https://doi.org/10.1016/S0191-8141(00)00042-0

Pearce, M. A., Wheeler, J., & Prior, D. J. (2011). Relative strength of mafic and felsic rocks during amphibolite facies metamorphism and deformation. *Journal of Structural Geology*, *33*(4), 662–675. https://doi.org/10.1016/j.jsg.2011.01.002

Pieri, M., Burlini, L., Kunze, K., Stretton, I., & Olgaard, D. L. (2001). Rheological and microstructural evolution of Carrara marble with high shear strain: Results from high temperature torsion experiments. *Journal of Structural Geology*, *23*(9), 1393–1413. https://doi.org/10.1016/S0191-8141(01)00006-2

Pieri, M., Kunze, K., Burlini, L., Stretton, I., Olgaard, D. L., Burg, J.-P., & Wenk, H.-R. (2001). Texture development of calcite by deformation and dynamic recrystallization at 1000 K during torsion experiments of marble to large strains. *Tectonophysics*, *330*(1–2), 119–140. https://doi.org/10.1016/S0040-1951(00)00225-0

Popov, A. A., & Sobolev, S. V. (2008). SLIM3D: A tool for three-dimensional thermomechanical modeling of lithospheric deformation with elasto-visco-plastic rheology. *Physics of the Earth and Planetary Interiors*, *171*(1–4), 55–75. https://doi.org/10.1016/j.pepi.2008.03.007

Popov, A. A., Sobolev, S. V., & Zoback, M. D. (2012). Modeling evolution of the San Andreas fault system in northern and central California. *Geochemistry, Geophysics, Geosystems*, *13*, Q08016. https://doi.org/10.1029/2012GC004086

Quinteros, J., & Sobolev, S. V. (2013). Why has the Nazca plate slowed since the Neogene? *Geology*, *41*(1), 31–34. https://doi.org/10.1130/G33497.1

Quinteros, J., Sobolev, S. V., & Popov, A. A. (2010). Viscosity in transition zone and lower mantle: Implications for slab penetration. *Geophysical Research Letters*, *37*, L09307. https://doi.org/10.1029/2010GL043140

Rybacki, E., Morales, L. F. G., Naumann, M., & Dresen, G. (2014). Strain localization during high temperature creep of marble: The effect of inclusions. *Tectonophysics*, *634*, 182–197. https://doi.org/10.1016/j.tecto.2014.07.032

Schmeling, H., Marquart, G., & Grebe, M. (2018). A porous flow approach to model thermal non-equilibrium applicable to melt migration. *Geophysical Journal International*, *212*(1), 119–138. https://doi.org/10.1093/gji/ggx406

Schmid, S. M., Boland, J. N., & Paterson, M. S. (1977). Superplastic flow in finegrained limestone. *Tectonophysics*, *43*(3–4), 257–291. https://doi.org/10.1016/0040-1951(77)90120-2

Schmid, S. M., Paterson, M. S., & Boland, J. N. (1980). High temperature flow and dynamic recrystallization in Carrara marble. *Tectonophysics*, *65*(3–4), 245–280. https://doi.org/10.1016/0040-1951(80)90077-3

Simo, J. C., & Hughes, T. J. (2006). *Computational inelasticity*, (Vol. 7). New York: Springer-Verlag.

Tasaka, M., Zimmerman, M. E., Kohlstedt, D. L., Stünitz, H., & Heilbronner, R. (2017). Rheological weakening of olivine + orthopyroxene aggregates due to phase mixing: Part 2. Microstructural development. *Journal of Geophysical Research: Solid Earth*, *122*, 7597–7612. https://doi.org/10.1002/2017JB014311

Ter Heege, J. H., De Bresser, J. H. P., & Spiers, C. J. (2001). The influence of dynamic recrystallization on the grain size distribution and rheological behaviour of Carrara marble deformed in axial compression. *Geological Society, London, Special Publications*, *200*(1), 331–353. https://doi.org/10.1144/GSL.SP.2001.200.01.19

Thielmann, M., & Kaus, B. J. P. (2012). Shear heating induced lithospheric-scale localization: Does it result in subduction? *Earth and Planetary Science Letters*, *359-360*, 1–13. https://doi.org/10.1016/j.epsl.2012.10.002

Treagus, S. H., & Lan, L. (2004). Deformation of square objects and boudins. *Journal of Structural Geology*, *26*(8), 1361–1376. https://doi.org/10.1016/j.jsg.2003.12.002

Valoroso, L., Chiaraluce, L., Piccinini, D., Di Stefano, R., Schaff, D., & Waldhauser, F. (2013). Radiography of a normal fault system by 64,000 high-precision earthquake locations: The 2009 L'Aquila (central Italy) case study. *Journal of Geophysical Research: Atmospheres*, *118*, 1156–1176. https://doi.org/10.1002/jgrb.50130

Warren, J. M., & Hirth, G. (2006). Grain size sensitive deformation mechanisms in naturally deformed peridotites. *Earth and Planetary Science Letters*, *248*(1–2), 438–450. https://doi.org/10.1016/j.epsl.2006.06.006

Webber, S., Ellis, S., & Fagereng, Å. (2018). "Virtual shear box" experiments of stress and slip cycling within a subduction interface mélange. *Earth and Planetary Science Letters*, *488*, 27–35. https://doi.org/10.1016/j.epsl.2018.01.035

White, S. (1976). A discussion on natural strain and geological structure—The effects of strain on the microstructures, fabrics, and deformation mechanisms in quartzites. *Philosophical Transactions for the Royal Society of London A.*, *283*(1312), 69–86. https://doi.org/10.1098/rsta.1976.0070

Zang, A., Wagner, F. C., Stanchits, S., Janssen, C., & Dresen, G. (2000). Fracture process zone in granite. *Journal of Geophysical Research*, *105*, 23,651–23,661. https://doi.org/10.1029/2000JB900239